

VIP Very Important Paper



Metal-Nitrogen-Carbon Cluster-Decorated Titanium Carbide is a Durable and Inexpensive Oxygen Reduction Reaction Electrocatalyst

Sung Beom Cho^{+, [a, b]} Cheng He⁺,^[c] Shrihari Sankarasubramanian⁺,^[c] Arashdeep Singh Thind,^[d] Javier Parrondo,^[c] Jordan A. Hachtel,^[e] Albina Y. Borisevich,^[e] Juan-Carlos Idrobo,^[e] Jing Xie,^[c] Vijay Ramani,*^[c, d] and Rohan Mishra*^[a, d]

Clusters of nitrogen- and carbon-coordinated transition metals dispersed in a carbon matrix (e.g., Fe–N–C) have emerged as an inexpensive class of electrocatalysts for the oxygen reduction reaction (ORR). Here, it was shown that optimizing the interaction between the nitrogen-coordinated transition metal clusters embedded in a more stable and corrosion-resistant carbide matrix yielded an ORR electrocatalyst with enhanced activity and stability compared to Fe–N–C catalysts. Utilizing first-principles calculations, an electrostatics-based descriptor of catalytic activity was identified, and nitrogen-coordinated iron (FeN_4) clusters embedded in a TiC matrix were predicted to be

an efficient platinum-group metal (PGM)-free ORR electrocatalyst. Guided by theory, selected catalyst formulations were synthesized, and it was demonstrated that the experimentally observed trends in activity fell exactly in line with the descriptor-derived theoretical predictions. The Fe–N–TiC catalyst exhibited enhanced activity (20%) and durability (3.5-fold improvement) compared to a traditional Fe–N–C catalyst. It was posited that the electrostatics-based descriptor provides a powerful platform for the design of active and stable PGM-free electrocatalysts and heterogenous single-atom catalysts for other electrochemical reactions.

Introduction

Polymer electrolyte fuel cells (PEFCs) combine hydrogen and oxygen to generate electricity and water. Due to their high power and their ability to decouple power and energy, they are a promising technology for clean, portable power applications such as in automotive transportation. However, the biggest hurdle for their widespread commercialization is the lack of a low-cost and durable electrocatalyst^[1] to

promote the sluggish oxygen reduction reaction (ORR) at the cathode. The ORR in current PEFCs is catalyzed by expensive platinum-group-metal (PGM)-based nanoparticles dispersed on carbon supports.^[2] The benchmark ORR activity of platinum and platinum alloys combined with the low cost, abundance, high electronic conductivity (30 S cm^{-1}), and high surface area ($200\text{--}300 \text{ m}^2 \text{ g}^{-1}$) of carbon supports renders Pt/C as the catalyst of choice for commercial PEFCs.^[3,4] The optimization of Pt/C catalysts is ongoing, largely following a roadmap described by Gasteiger et al.^[5] to reduce Pt loadings from 0.4–0.8 to about $0.1 \text{ mg}_{\text{Pt}} \text{ cm}^{-2}$, but further progress is impeded by deteriorating performance with lower Pt loading that ensures minimal stack level cost reductions.^[6] An alternate strategy to substantially reduce PEFC costs is to replace Pt with cheaper catalysts.

Candidates for PGM-free catalysts include a variety of transition metal-nitrogen (TMN) clusters inspired by early work on iron porphyrins and cobalt phthalocyanines adsorbed on graphite,^[7,8] carbon nanocomposites,^[9] transition metal carbides,^[10] and transition metal nitrides.^[10,11] Amongst these, TMN clusters in carbon matrices have emerged as a promising class of PGM-free catalysts with excellent ORR activity.^[12–19] In the past decade, a variety of methods have been used to prepare these catalysts,^[16–18,20] and highly active single Co^[21] or Fe^[22] atom catalysts with four-fold N coordination^[17] in carbonaceous matrices have been demonstrated. As these TMN catalysts are composed of earth-abundant metals, they are expected to overcome the cost issue of PGM catalysts.

Besides cost, the durability of ORR catalysts is the second major bottleneck, especially for automotive applications. The durability of current ORR catalysts, including TMN catalysts in

[a] Dr. S. Beom Cho,⁺ Prof. R. Mishra
Department of Mechanical Engineering and Materials Science
Washington University in St. Louis
St. Louis, Missouri 63130 (USA)
E-mail: rmishra@wustl.edu

[b] Dr. S. Beom Cho⁺
Virtual Engineering Center, Technology Convergence Division
Korea Institute of Ceramic Engineering and Technology (KICET)
Jinju 52851 (South Korea)

[c] Dr. C. He,⁺ Dr. S. Sankarasubramanian,⁺ Dr. J. Parrondo, J. Xie,
Prof. V. Ramani
Department of Energy, Environment and Chemical Engineering
Washington University in St. Louis
St. Louis, Missouri 63130 (USA)
E-mail: ramani@wustl.edu

[d] A. Singh Thind, Prof. V. Ramani, Prof. R. Mishra
Institute of Materials Science and Engineering
Washington University in St. Louis
St. Louis, Missouri 63130 (USA)

[e] Dr. J. A. Hachtel, Dr. A. Y. Borisevich, Dr. J.-C. Idrobo
Center for Nanophase Materials Sciences
Oak Ridge National Laboratory
Oak Ridge, TN 37830 (USA)

[+] These authors contributed equally to this work.

 Supporting information for this article is available on the WWW under
<https://doi.org/10.1002/cssc.202101341>

carbon matrices is far from that required to obtain a targeted range of 8000 h operation (equivalent to a range of 150000 miles for an automotive stack) with less than 10% loss of performance.^[23] Spikes in voltage, temperature, and humidity during the operation of a PEFC results in degradation after only a few hundred to a few thousand cycles.^[24–26] This lack of durability is primarily due to the corrosion of carbon.^[27] In particular, under automotive fuel cell stack start-up/shut-down conditions, the cathode is exposed to spikes in potential as high as 1.5–2.0 V,^[28] which results in irreversible carbon corrosion. Through such repeated start-up/shut-down cycles, inevitable during daily operation, carbon undergoes breakdown and loss of porosity resulting in reduced surface area. This problem is compounded by the loss of active sites, either Pt nanoparticles or TMN clusters, as they can get detached from the carbon support or matrix and/or undergo agglomeration,^[26,27] both of which critically degrade the ORR activity. Higher durability in Pt-based ORR catalysts has been obtained by dispersing Pt nanoparticles over corrosion-resistant supports, such as doped TiO₂, doped SnO₂, and other metal oxides that can withstand the voltage spikes during start-up/shut-down cycles.^[29–36] In TMN-catalysts, since the TMN-clusters are directly embedded in the matrix, there is a strong effect of the matrix on the stability and ORR activity of the embedded clusters.^[37,38] Given the large choice of available TMN clusters coupled with a modest selection of available stable electrocatalyst matrices,^[9,39] there is a need for a rational design approach that accounts for active site-matrix interactions to enable efficient identification of TMN cluster/matrix systems having the most promising combination of ORR activity and durability.

In this study, we employed an approach based on first-principles density functional theory (DFT) calculations to rapidly screen through a large set of TMN clusters (TM=Mn, Fe, Co, Ni, Zn, Zr, and Mo) embedded in corrosion-resistant TiC matrices that have a good combination of stability, surface area, and conductivity. We predict FeN₄ clusters in TiC to be an inexpensive and durable catalyst having better performance than TMN clusters in carbon (graphene) matrices. This catalyst formulation was obtained by developing a scaling relation based on the electrostatic interactions between TiC and the TMN clusters. To validate our theoretical predictions, we synthesized various TMN catalysts embedded in TiC. We characterized their structure and composition using a suite of techniques including X-ray photoelectron spectroscopy (XPS), scanning electron microscopy (SEM), aberration-corrected scanning transmission electron microscope (STEM) imaging, and electron energy loss spectroscopy (EELS) to show successful incorporation of the catalytically active clusters into the TiC matrix. The measured ORR activity of these catalysts precisely confirmed our electrostatics-based theoretically predicted scaling relation. Moreover, upon comparing an electrocatalyst comprising Fe–N clusters in TiC with a baseline Fe–N cluster in carbon electrocatalyst synthesized using the same method, we found that Fe–N–TiC exhibited an ORR activity [2.3 mA cm⁻² at the half-wave potential ($E_{1/2}$)] that was 20% greater than Fe–N–C

(1.85 mA cm⁻² at $E_{1/2}$) and comparable to the literature^[40–42] while also retaining 50% greater activity than Fe–N–C following 1000 cycles of the stringent accelerated catalyst corrosion resistance protocol^[43] adopted by the US Department of Energy and most major automotive companies.

Results and Discussion

An ideal corrosion-resistant support or matrix that is stable under typical start-up/shut-down conditions should have an oxidation potential above 1.5 V. It should also have good electronic conductivity and high surface area. We used TiC as the corrosion-resistant matrix of choice as it has an oxidation potential of 1.75 V and is expected to be stable under the acidic conditions present in a PEFC according to its surface-Pourbaix diagram.^[44] Furthermore, TiC has a work function of 4.6 eV, similar to that of graphene (4.62 eV),^[45] and a low resistivity of 0.003 Ω m,^[46] which is beneficial to mimic the electronic conductivity of carbon.^[17] It has been previously used as an alternative to graphite supports for electrocatalysts.^[47,48] TiC has a rock-salt structure with the (001) surface being the most stable, having a low surface energy of 0.098 eV Å⁻².

To identify TMN clusters with the best ORR activity, we explored seven different TM cations including Mn, Fe, Co, Ni, Zn, Zr, and Mo. We varied the position of the TM and N atoms as they can either be present as ad-atoms on the (001) TiC surface or could substitute the surface Ti and C atoms, respectively. They could also be present as substitutional atoms within the bulk. Furthermore, the stoichiometry (x) of the TM–N_x clusters can vary from 0–4. We calculated the formation energy of all the above possible combinations under various chemical potentials. We found TM–N₄ clusters substituting the surface Ti–C atoms, as shown in Figure 1a, to be the most stable configuration for a wide range of chemical potentials. We also found that the TM–N₄ clusters in TiC matrices were more stable than those in graphene matrices. For instance, the formation energy of a FeN₄ cluster substituting the surface Ti and C atoms of TiC is –5.6 eV, compared to –3.1 eV in graphene matrices. A lower formation energy of the TM–N₄ clusters on TiC suggests a smaller tendency to detach from TiC matrices than from graphene/carbon.

As the TM–N₄ clusters are directly embedded on the TiC matrix, their catalytic activity will be affected by the electronic structure of the matrix. Despite the metallic nature of both graphene and TiC, the bonding in TiC is more ionic, which can be observed from the difference in the projected electrostatic potential of the two materials with embedded FeN₄ clusters as shown in Figure 1a,b. On graphene, the TM site shows a higher potential as shown in the corresponding line profile in Figure 1b and is expected to have stronger electrostatic attraction towards electrons than the surrounding carbon or nitrogen atoms. On TiC, however, the Ti sites surrounding the FeN₄ cluster show comparable electrostatic potential to the Fe ion. We find that the Ti sites have a higher affinity to attract electrons than all of the TMs examined here, except for Zr and Mo (see the Supporting Information). This, in turn, results in

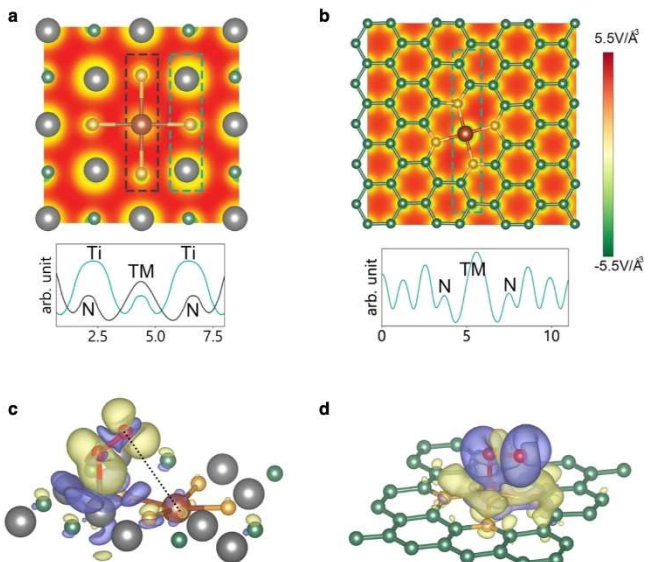


Figure 1. Atomic configuration of the FeN₄–TiC catalyst. (a) Atomic model of FeN₄–TiC overlaid on the electrostatic potential. (b) Atomic configuration of FeN₄ cluster on graphene support overlaid on the electrostatic potential. The insets below show the planar-averaged electrostatic potential profiles from the selected regions shown in (a,b) with dashed boxes. Charge-difference plot of O₂ adsorbed on (c) FeN₄ on TiC and (d) FeN₄ on graphene with pristine substrates. Blue color represents accumulated electrons while the yellow color represents depleted electrons. The isosurface level is set to 0.001 e Å⁻³. The black dotted line in (c) indicates the electrostatic interaction between O₂ and Fe. The grey, green, brown, yellow, red, and white circles represent Ti, C, Fe, N, O, and H atoms, respectively.

different adsorption mechanisms on the two matrices. On graphene, O₂ adsorbate molecules attach to the TM ion, which serves as the active site for ORR.^[49] On TiC, the adsorbates prefer binding to the Ti site neighboring the TM–N₄ clusters for most metals, except Zr and Mo. We note that the TM–N₄ clusters modulate the electronic structure of the Ti atoms, and consequently, contribute to the energetics of the adsorbates.

To screen the best possible combination of TM–N₄ clusters embedded in TiC, it is necessary to optimize the binding energy of the adsorbates on the active sites such that they follow the Sabatier principle,^[50] that is, the binding energy is neither too weak to hinder adsorption nor too strong to prevent the desorption of the product. By combining DFT binding energies of various ORR intermediates with the computational hydrogen electrode approach,^[51] we calculated the ORR activity of different TM–N₄ clusters. We allowed for the adsorbates to bind to either the Ti or the TM sites and the possibility to form H₂O₂, instead of H₂O. While the rate-limiting step varied with the TM ions, we found the FeN₄ clusters to show the highest activity amongst the selected TM ions. The adsorbates preferred binding to the Ti atom next to FeN₄ clusters and the rate-limiting step was the step involving O+(H⁺+e⁻)→OH. The overpotential, η_{eff} , is determined by the difference between the limiting potential (U_{rl}) and the equilibrium potential (1.23 V). This analysis also allows us to conclusively state that N sites are not preferred for ORR due to the very strong binding of OH intermediates to those sites (see Figure S6 in the Supporting

Information). This prevents the further progress of the reaction to produce water.

It is computationally prohibitive to calculate the ORR activity of all the available 3d and 4d TM elements to identify the one with the highest ORR activity. Scaling relations that are computationally less demanding to calculate or measure experimentally provide an efficient route to identify promising catalysts. Scaling relations are commonly based on descriptors, such as the work function of the catalyst,^[52] or the center of the d-band from the Fermi energy in the case of TM alloys and compounds.^[53] Following the Sabatier principle, activity is observed to increase as a function of the descriptor to reach a maximum value, after which it decreases, thus giving an overall appearance of a volcano.^[54] As shown in Figure 2a, the overpotential of TM–N₄ clusters in TiC, a signature of their ORR activity (from polarization curves in Figure S9 in Supporting Information), showed a volcano-like relation as a function of the binding energy of the rate-limiting intermediate OH. We found that the ORR activity of the calculated set of TMs did not show any correlation with the d-band center of the TM ions. Instead, we found that the calculated ORR activity scaled linearly with

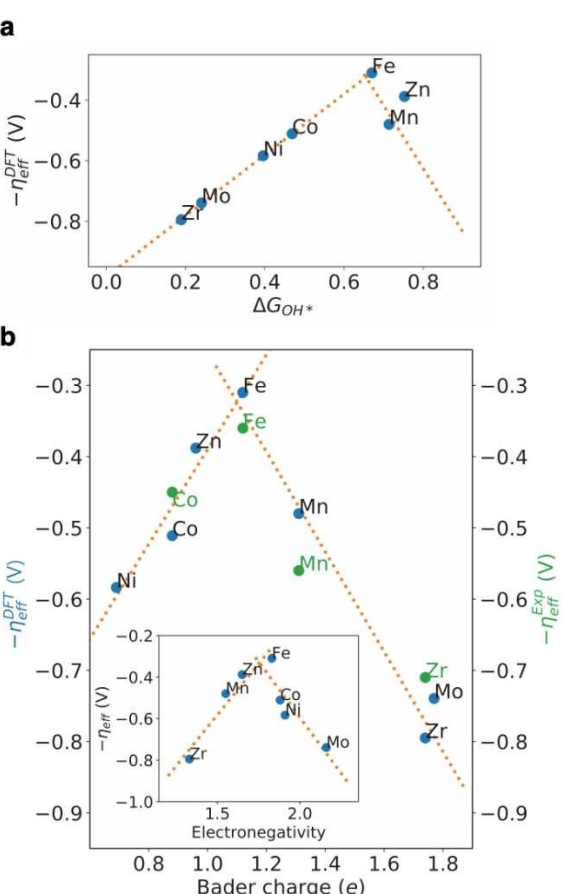


Figure 2. Scaling relations for TMN₄–TiC catalysts. Trends of overpotential as a function of (a) the binding energy of OH⁻ intermediates and (b) the calculated Bader charge of Ti for various TM–N₄ clusters. The experimentally measured overpotentials are marked with green color in (b). Inset of (b) shows the trends as a function of electronegativity of the TM atom.

the electrostatic interaction between the TM and Ti ions through the bridging N ions.

To quantitatively capture the electrostatic interaction, we calculated the Bader charge of the various atoms.^[55] Bader charge analysis is a method to partition the valence electrons by integrating the charge density within a volume defined by the zero-flux surface around every atom. For the seven TMs, we found that the maximum overpotential for the complete ORR process showed a volcano-like relationship with the Bader charge of the TM atom, as seen in Figure 2b. This implies that the ORR activity for this class of TM–N₄ catalysts in TiC can be predicted based on the electrostatic interaction and Bader charges of the cluster and the matrix, which allows one to avoid computationally intensive DFT calculation of the entire ORR reaction on every TM cluster. As noted before, even though the adsorbates are attached to the Ti site, the adjacent TM–N₄ cluster strongly affects the binding energy (see the Supporting Information). In the absence of any TM–N₄ clusters, the binding energies are too weak and the overpotential on bare TiC substrate is 1.04 V. On the other hand, the N-doped TiC substrate (without TM atoms) binds too strongly to the adsorbates. The TM atom in the TM–N₄ cluster plays a central role in mellowing the binding energy. Given the electrostatic nature of interaction between TM, Ti, and the adsorbates, we find that the Bader charge of the TM atom, which captures its ionicity, shows descriptive behavior.

Moreover, as Fe lies at the peak of the volcano plot, we predicted it to be the most efficient TM among 3d and 4d TM elements. We also found that a readily accessible elemental descriptor, the electronegativity of the TM atom, also showed a volcano-like relation with the overpotential. The dominant role played by electrostatics in determining the ORR activity in this class of PGM-free catalysts is in stark contrast to PGM catalysts, where the adsorption energetics strongly depend on spd-covalency. While these electrostatics-based descriptors cannot predict all the details of ORR, they are expected to be useful to accelerate the screening process from the large combination of available TMN clusters and matrices.

To confirm the theoretical prediction of achieving Fe–N–TiC catalysts with high activity and durability, and to verify the predicted scaling relations, we synthesized a variety of TMN catalysts in C and TiC matrices using a wet impregnation method described in greater detail in the Experimental Section. This method has been previously employed to synthesize a variety of PGM-free catalysts.^[16,56] The precursors were imbibed into the pores of the matrices by capillary action. Subsequent annealing in a furnace resulted in the formation of the TMN complexes (confirmed by XPS). The electrochemical performance of the catalysts was evaluated using a thin-film rotating disk electrode (tf-RDE) as detailed in the Experimental Section. The experimental overpotentials ($\eta_{\text{eff}}^{\text{Exp}}$) were calculated based on the onset potential for the ORR and the equilibrium potential. The trend measured experimentally was found to closely track the DFT predictions based on the Bader charge descriptor, as seen in Figure 2b.

We characterized the Fe–N–TiC samples using XPS. A high-resolution XPS spectrum of N1s orbital was measured

and fitted as depicted in Figure 3. Upon deconvolution, the presence of a peak centered around 399 eV indicated the presence of TM–N_x metal coordinated moieties in case of all four TMN–TiC catalysts.^[57,58] Significant amounts of graphitic-N (\approx 401.1 eV) as opposed to either the pyridinic-N or pyrrolic-N forms were observed in line with prior reports that annealing at higher temperatures increases the proportion of graphitic-N.^[21] This was also verified by comparing the XPS spectrum of baseline Fe–N–C catalyst as shown in Figure 3b. Further, we observed evidence of the formation of Ti–N as indicated in Figure 3.^[59] Thus, the XPS results indicated the formation of TM–N_x moieties for all the TMs considered. The associated graphitic-N and Ti–N groups indicated the N-doping of the TiC matrix. We also characterized the Fe–N–TiC samples using X-ray diffraction (XRD). Despite only a few atoms of the metal being coordinated with N atoms (by design) in each cluster and being present on the TiC substrate, we were able to observe the formation of distinct and characteristic diffraction patterns for Fe and TiC as seen in Figure S7 without evidence of additional phases. Complementing this, we have used atomic resolution microscopy to demonstrate the synthesis of these single- or few-atom clusters on TiC as detailed below.

To further verify the incorporation of Fe–N clusters into the surfaces of the TiC nanoparticles, we performed atomic-resolution STEM imaging and EELS. We used the high-angle annular dark field (HAADF) imaging mode in STEM to determine the size and shape of the TiC nanoparticles. In HAADF images, the intensity is approximately proportional to Z² of the atomic columns, with Z being the atomic number.^[60] We found the TiC nanoparticles were highly faceted and randomly oriented, as shown in Figure 4a, with their sizes varying from 20 to 65 nm. To gain insight into the chemical composition of the TiC nanoparticles and to ascertain the successful incorporation of Fe and N, we used EELS imaging. Previous experiments have shown that lower concentration elements are easier to detect using STEM-EELS along near-surface regions.^[13,61] Hence, we have characterized the near-surface region of several TiC nanoparticles to understand the extent and distribution of Fe and N atoms in TiC. A low-resolution HAADF image of the near-surface region of a representative TiC nanoparticle is shown in Figure 4b. Figure 4c shows an atomic-resolution HAADF image of a selected region of the nanoparticle that has been highlighted with a white box in Figure 4b. This area was used to record a representative EELS image. Figure 4d shows a set of elemental edge maps extracted from the spectrum image showing the distribution of C, N, Ti, and Fe in the selected region. From Ti L and C K edge maps, it is clear that the bulk of the nanoparticle was primarily composed of these two elements. The segregation of Fe and N to form clusters at the surface could be clearly observed in Fe L and N K edge maps, respectively, where the intensities are brighter closer to the surface than in the bulk of the nanoparticle. The background-subtracted core-loss edges of the four elements along with the energy ranges over which the respective signals were integrated to obtain the elemental edge maps are shown in

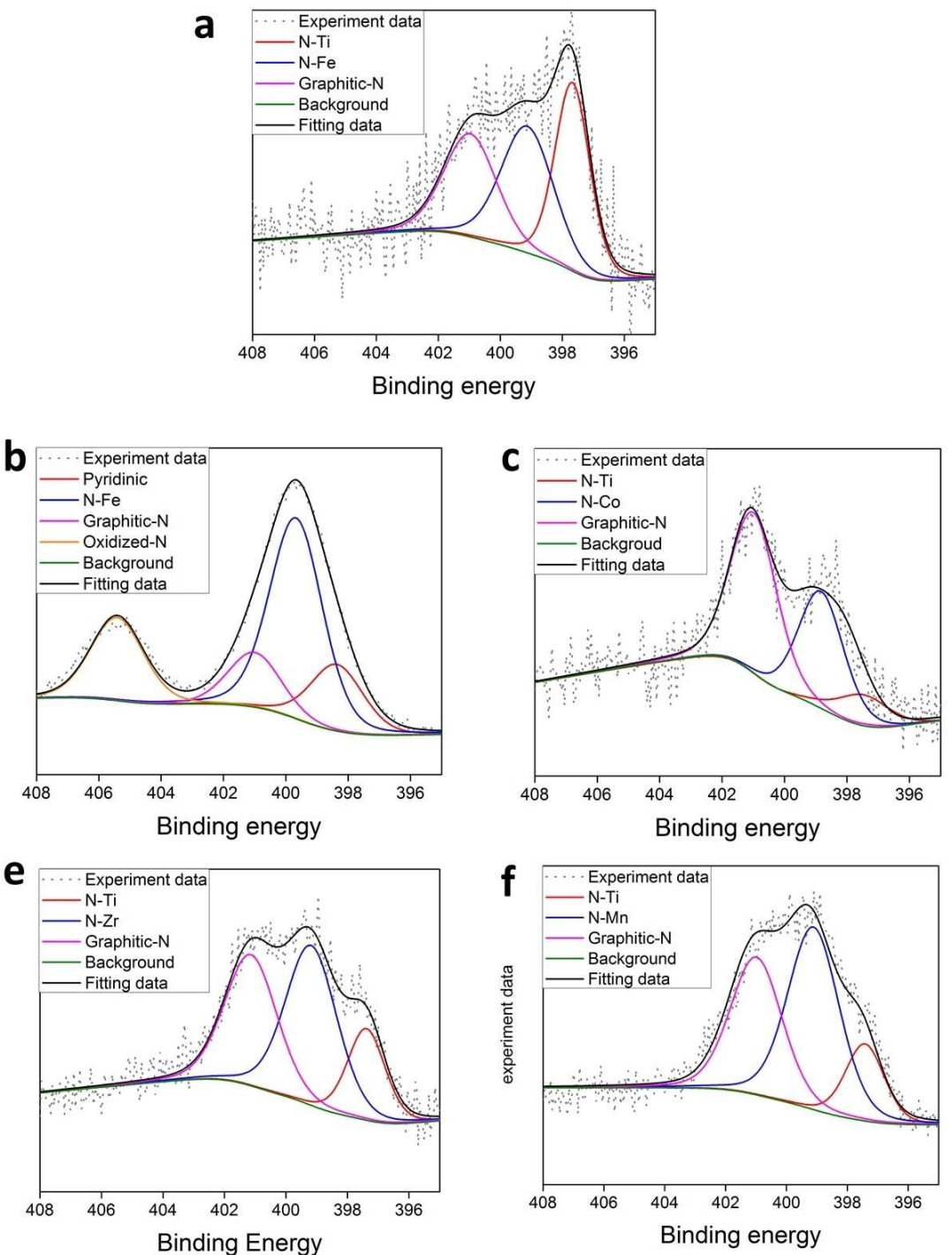


Figure 3. XPS characterization of TMN–TiC catalysts. The deconvoluted peaks depict the N–Ti, N–TM, and C–N bonds in (a) $\text{FeN}_4\text{-TiC}$, (b) FeN_4/C , (c) $\text{CoN}_4\text{-TiC}$, (d) $\text{ZrN}_4\text{-TiC}$, and (e) $\text{MnN}_4\text{-TiC}$.

Figure 4e for a region highlighted by the black box in Figure 4c.

Fe–N–C and Fe–N–TiC catalysts were chosen for further ORR activity evaluation. Fe–N–TiC exhibited a current density of 2.3 mA cm^{-2} at $E_{1/2}$ vs. standard hydrogen electrode (SHE), which was comparable to reports on Fe–N–C in the literature.^[40–42] As depicted in Figure 5a, Fe–N–TiC exhibited

higher activity compared to Fe–N–C (2.3 vs. 1.85 mA cm^{-2} at $E_{1/2}$ vs. SHE). The experimentally observed higher activity of Fe–N–TiC is in excellent agreement with the theoretically predicted smaller deviation of free energy from the ideal ORR energy path for Fe–N–TiC compared to Fe–N–C as shown in Figure 5b. Further, the durability of these catalysts was evaluated using an accelerated catalyst corrosion resistance

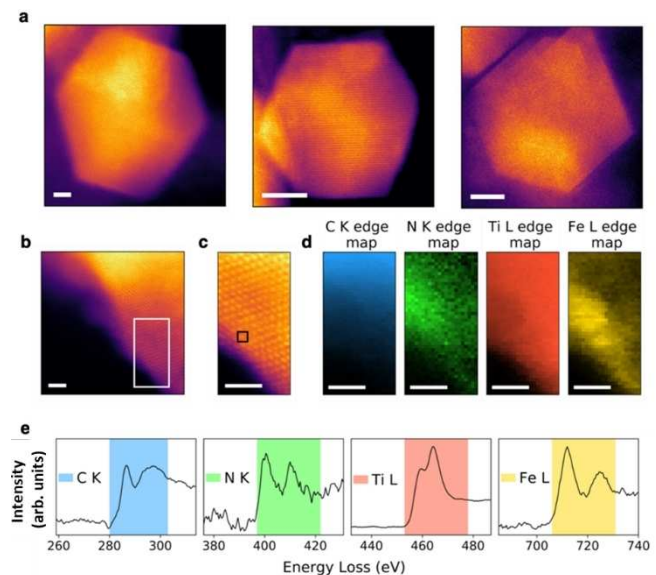


Figure 4. STEM imaging and EEL spectra of $\text{FeN}_4\text{-TiC}$ catalysts. (a) HAADF images of TiC nanoparticles. (b) Low-resolution HAADF image showing a nanoparticle. The white box in (b) shows the region chosen for EELS data acquisition. (c) Simultaneously acquired HAADF image of the region highlighted in (b). A 16×16 sub-pixel scanning was enabled during acquisition. (d) Integrated intensity maps of Ti, C, Fe, and N core-loss edges. (e) Extracted EEL spectra of corresponding elements after PCA and subsequent background subtraction from the selected region in (c) marked with a black box. Scale bars correspond to 5 nm for (a) and 2 nm for (b-d).

protocol.^[43] This protocol mimicked the high-voltage transients encountered during the start-up and shut-down of a fuel cell where the aggressive “hydrogen-front” mechanism^[62] can result in significant oxidation of carbonaceous materials and the subsequent aggregation or loss of catalyst. The change in activity and capacitance of the catalysts after 1000 cycles of this protocol was used to evaluate the long-term stability of these catalysts. The Fe-N-TiC lost 13% of its activity over the course of this test as compared to a 46% activity loss for the Fe-N-C catalyst as seen from the inset in Figure 5a. The ORR kinetic currents on these catalysts at the beginning of life (BoL, before the accelerated catalyst corrosion resistance protocol) and the end of life (EoL, after the accelerated corrosion resistance protocol) were calculated using the Koutecky-Levich equation.^[63] The increase in overpotential applied to achieve a kinetic current density of 0.1 mA cm^{-2} on Fe-N-C over the course of this test was 5× the increase observed on Fe-N-TiC , demonstrating the superior corrosion resistance of Fe-N-TiC . There is a lack of consensus on the best metric to evaluate PGM-free catalysts, which is further compounded by the variety of test conditions (type of counter electrode, electrolyte composition).^[64] Variations in the particle sizes of catalysts results in different thickness and morphology of the tf-RDEs, leading to different flow regimes at the electrode surface and making direct comparison between reports in the literature challenging. Thus, we have provided three different metrics to evaluate catalyst durability in terms of increase in over-

potential, current density at $E_{1/2}$, and mass activity at a 100 mV overpotential (see Figure S8) and show that the Fe-N-TiC catalysts are more stable than Fe-N-C catalysts when evaluated by all three metrics. Figure 5c depicts the cyclic voltammograms (CVs) recorded with the pristine catalyst and after 1000 catalyst corrosion resistance stability cycles on Fe-N-TiC and Fe-N-C , respectively. Both catalysts display a decrease in capacitive currents in their CVs indicative of a decrease in their electrochemically active surface area (ECSA). Fe-N-C showed a 22% loss of ECSA over the course of the catalyst corrosion resistance stability test compared to Fe-N-TiC , which lost only 4% of its initial ECSA. The greater stability of Fe-N-TiC was directly ascribed to improved matrix stability.

Conclusions

We have identified Fe-N-TiC catalysts as active and durable class of platinum-group metal (PGM)-free catalysts. Our study suggests the important role that the PGM-free catalyst matrix plays both on the activity and durability of this class of catalysts. The higher durability of these catalysts arises from the TiC matrix, which is resistant to corrosion at the high potential spikes that occur during start-up/shut-down conditions in an automotive fuel cell stack. Under such aggressive conditions, Fe-N catalysts on conventional carbon-based supports suffer from corrosion that is irreversible in nature. In future, the activity of the proposed, durable Fe-N-TiC catalysts can be further improved by optimizing the growth and processing conditions, including the use of TiC matrices with higher surface area, such as nanowires and nanosheets, doping of the matrix to improve electrical conductivity, alloying one or more transition metal elements in the clusters. Furthermore, the electrostatics-based descriptor proposed here can be an efficient strategy to screen active catalysts on other corrosion-resistant and conductive matrices with high surface area, and to design clusters including more than one transition metal element.

Experimental Section

Computational details

The first-principles DFT calculations were performed using the Vienna ab-initio Simulation Package (VASP)^[65] with the projector augmented-wave (PAW) method.^[66] The plane-wave basis set was expanded to a cutoff energy of 400 eV and the Perdew-Burke-Ernzerhof (PBE) functional^[67] was adopted to describe the exchange-correlation interactions. A slab model was constructed with 6 layers of (2×2) TiC unit cell having (001) surfaces on the top and the bottom. Atoms in the bottom two layers were fixed to the optimized bulk positions. At least 15 Å of vacuum was inserted to minimize the interaction between periodic slabs. The structural optimization was performed with a force criterion of 0.01 eV \AA^{-1} . A k -points mesh of $(9 \times 9 \times 1)$ was used with the Monkhorst-Pack scheme^[68] to sample the Brillouin zone.

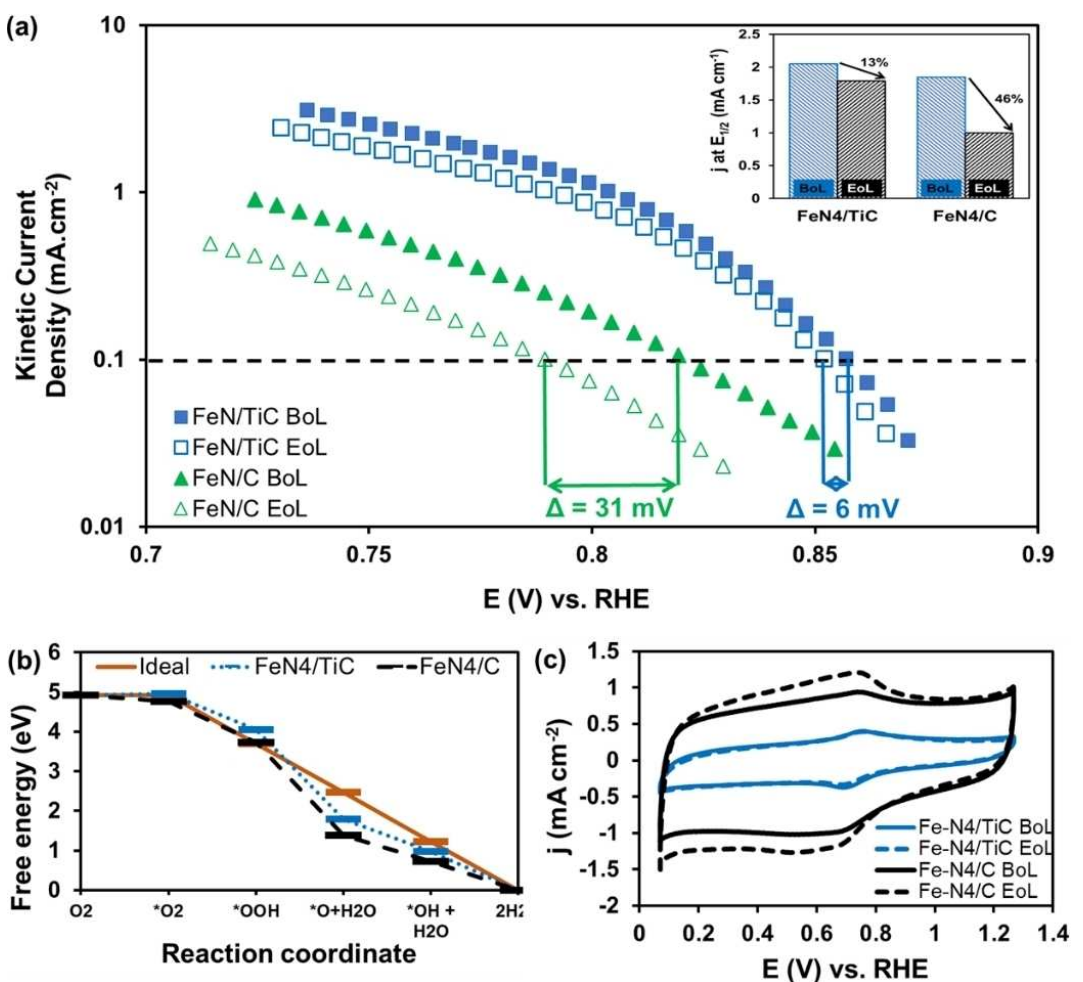


Figure 5. Effect of catalyst support on activity and durability of FeN_4 catalysts. (a) Kinetic currents extracted from linear sweep voltammograms of $\text{FeN}_4\text{-TiC}$ and $\text{FeN}_4\text{-C}$ catalysts at beginning of life (BoL) and end of life (EoL), measured with a 20 mV s^{-1} sweep rate and 1600 RPM rotation rate in $0.5 \text{ M H}_2\text{SO}_4$ with 1 mg cm^2 catalyst loading showing the increase in overpotential needed to output 100 mA cm^{-2} due to catalyst degradation. Inset depicts the activity at $E_{1/2}$ for both catalysts at BoL and EoL. (b) DFT-calculated free-energy diagram of $\text{FeN}_4\text{-TiC}$ and $\text{FeN}_4\text{-C}$ for ORR. The computational hydrogen electrode assumes acidic condition with $\text{pH}=0$, and the cell potential in our free-energy calculation is set to 1.23 V (c) Cyclic voltammograms of the Fe-N-C and Fe-N-TiC catalysts in their pristine state and after 1000 cycles of the catalyst corrosion resistance stability protocol.

To test the behavior of single TM atoms on TiC, their formation energies, E_f (TM@TiC), were calculated using the following Equation (1):

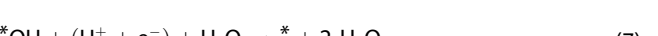
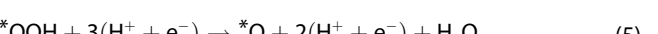
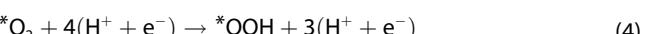
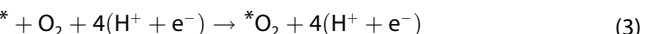
$$E_f(\text{TM@TiC}) = E_{\text{TM@TiC}} - E_{\text{TiC}} - \mu_{\text{TM}} + m\mu_{\text{Ti}} + n\mu_{\text{C}} \quad (1)$$

where $E_{\text{TM@TiC}}$ and E_{TiC} denote the calculated energy of the transition-metal-embedded TiC and pristine TiC slab, respectively, m and n correspond to the number of substituted Ti and C atoms from TiC, and μ_{TM} , μ_{Ti} , and μ_{C} refer to the chemical potential of the respective elements. To define the chemical potentials, we assumed that transition metal elements are in their standard state and TiC is under stoichiometric condition: $\mu_{\text{Ti}} + \mu_{\text{C}} = E_f(\text{TiC})$. We tested bulk substitution, surface substitution, and ad-atom cases with single atoms. The surface substitution was the most stable case; thereby we constructed the possible active sites based on surface substitution of TM and N. We also calculated the formation energy of TM-N_x complex on TiC, $E_f(\text{TM-N}_x\text{@TiC})$, using the following Equation (2):

$$E_f(\text{TM-N}_x\text{@TiC}) = E_{\text{TM-N}_x\text{@TiC}} - E_{\text{TiC}} - \mu_{\text{TM}} - x\mu_{\text{N}} + m\mu_{\text{Ti}} + n\mu_{\text{C}} \quad (2)$$

By increasing concentration of N, we found that TM-N_4 was the most stable configuration.

We used the computational hydrogen electrode approach^[51] to calculate the reaction energetics for ORR using the following set of reactions [Eqs. (3)–(7)]:



In the reactions above, a standalone $*$ represents the surface site of the catalyst, and a $*$ in front of a molecule represents the binding

atom adsorbed on the surface site. The energetics were calculated based on the free energy of the adsorbates and molecules. The adsorbates were relaxed from various initial orientations and the most stable configuration was used to calculate the energetics. A free-energy correction to the adsorption energy was applied using the harmonic oscillator approximation at 298.15 K from the obtained vibrational frequency.^[69] The chemical potential of the pair of proton and electron was estimated by the sum of hydrogen molecule and the applied electric potential, $\mu(H^+ + e^-) = 0.5 \mu(H_2) - eU$, using the computational hydrogen electrode approach.^[51] The computational hydrogen electrode assumes acidic condition with pH=0, and the cell potential in our free energy calculations is set to 1.23 V. The rate-limiting potential (U_r) was determined by the largest free energy change (ΔG_{\max}) among the intermediate reactions, and the overpotential (η_{eff}) was calculated by $\eta_{\text{eff}} = \exp(U_r/eT) - 1.23$, where k is the Boltzmann constant and T is the temperature.

Catalyst preparation

Materials: 4-Aminoantipyrine (reagent grade, Sigma-Aldrich), TiC [<200 nm particle size (TEM), Sigma-Aldrich], zirconium(IV) oxy-nitrate hydrate ($>98\%$, Sigma-Aldrich), manganese(II) nitrate hydrate ($>98\%$, Sigma-Aldrich), cobalt(II) nitrate hexahydrate ($>98\%$, Sigma-Aldrich), and iron(III) nitrate nonahydrate ($>98\%$, Sigma-Aldrich).

Synthesis procedure: The catalysts were prepared by wet impregnation method, for which a slurry of the nitrate salt of the desired metal (3.5 mmol) was impregnated along with a nitrogen source [4-aminoantipyrine (AA-Pyr, 7 mmol)] into the surface of the desired matrix (TiC or carbon, 0.5 g). First, a known mass of matrix was dispersed in water by ultrasonication. Then, the AA-Pyr was dissolved in acetone (50 mL), and the solution was added to the matrix suspension and ultrasonicated for 30 min. Finally, the nitrate salt of the desired transition metal was added to the matrix-AA-Pyr dispersion and ultrasonicated for 1 h. The AA-Pyr and metal salt were incorporated into the pores of the matrix material by capillary action. The AA-Pyr-metal nitrate mixture was deposited inside the matrix pores by drying overnight at 60 °C in a convection oven. The resulting solid was powdered and then annealed in a tube furnace at 850 °C for 3 h under a N₂ atmosphere.

Electrochemical characterization of the catalysts

The catalysts were characterized using a thin-film electrode where a thin layer of the catalyst was deposited onto a hard, glassy carbon (GC) substrate. The electrode was subsequently rotated in a controlled fashion in an electrolyte mimicking the acidic conditions in an PEMFC and the catalyst was evaluated across the entire spectrum of kinetic and mass transport-controlled regimes.

Preparation of the thin-film rotating disk electrode: The catalyst ink was prepared by dispersing 116 mg of the catalyst in a mixture of 2.5 mL of deionized water, 2.5 mL of isopropyl alcohol, and 900 μL of Nafion solution (5 wt% Nafion; 1100 EW; Solution Technologies, Mendenhall, PA). Following 10 min of ultrasonication (Qsonica Q700) in an ice bath, 10 μL of ink was deposited onto a polished GC disk electrode (5 mm diameter) and dried at room temperature. This procedure resulted in a loading of 1 mg cm⁻² disk on the GC electrode.

Electrochemical measurements: All electrochemical experiments were performed in a jacketed cell (Pine instruments, AKCELL3) filled with 0.5 M H₂SO₄ electrolyte, a carbon-rod counter electrode, and a saturated calomel reference electrode (Pine instruments, RREF0022, 0.241 V vs. SHE). All potentials reported in this paper were

converted to the reversible hydrogen electrode (RHE) scale using the relation $E_{\text{RHE}} = E_{\text{SCE}} + 0.3$ V. The CVs employed to determine the ECSA were obtained by scanning the working electrode potential between 0.08 and 1.2 V vs. RHE under N₂ saturation. The changes in the ECSA are proportional to the capacitive current measured in these CVs. Linear sweep voltammetry (LSV) was performed under O₂-saturated conditions at room temperature to measure the catalyst activity for the ORR. The potential window employed in the experiment was between 0.1–1.1 V vs. RHE and sweep rate was 20 mV s⁻¹ with a 1600 rpm rotation rate.

Evaluation of catalyst stability: The corrosion rate of the catalyst is greatly influenced by the operation conditions, with the cathode reaching a potential of 1.5 V vs. RHE by the “hydrogen-front” mechanism during fuel cell start-up and shut-down.^[62] The catalyst corrosion resistance stability protocol mimics these transients encountered during the star-up and shut-down of a fuel cell and was employed to evaluate the catalyst electrochemical stability. This protocol involves cycling the tf-RDE potential between 1–1.5 V vs. SHE at a scan rate of 500 mV s⁻¹ for 1000 cycles. The test was performed in N₂-saturated 0.5 M H₂SO₄ electrolyte at room temperature. Over the course of this stability test, any change in the ECSA was monitored by observing the change in the capacitive current using CV (scan rate of 20 mV s⁻¹) recorded periodically after 0, 50, 100, 200, 500, and 1000 cycles.

STEM characterization

STEM-EELS experiments were carried out using the aberration-corrected (equipped with fifth-order aberration corrector and a cold field emission electron gun) Nion UltraSTEM™ 100 (operating at 60 kV) at Oak Ridge National Laboratory. EEL spectra were acquired using a Gatan Enfina spectrometer, with a collection semi-angle of 48 mrad and an energy dispersion of 0.5 eV per channel. The nanocrystals, in a powdered form, were transferred to a lacey carbon TEM grid by dip casting. The TEM grids were baked at 160 °C in vacuum to remove excess solvent and surface impurities prior to STEM-EELS experiments. For the EEL spectra, we used a power law to subtract the background signal from the characteristic edges. To suppress random noise in the EELS data, we performed principal component analysis (PCA), which is a multivariate statistical analysis method. Using PCA, dimensionality of a data set can be reduced to a handful of principal components, which describe the chemical fingerprint (EELS edges) in the data set while removing the random-noise components.^[70] We have selected the first five principals to reconstruct the spectrum images.

XRD characterization

XRD was carried out on finely ground powder samples of the catalysts using a Rigaku DMaxB instrument between $2\theta = 15\text{--}60^\circ$ with a step size of 0.06° and a dwell time of 2 s.

Author Contributions

R.M. and V.R. conceived the project. S.B.C. and R.M. performed the theoretical calculations and wrote the main text of the manuscript. C.H., S.S., J.P. and V.R. performed the catalysts synthesis and activity evaluation. S.S., C.H. and J.X. carried out the structural characterization of the catalysts. A.S.T. performed all STEM experiments with assistance from J.A.H., A.Y.B., J.C.I. and R.M.. All the authors discussed the results and contributed

to the revision of the manuscript. The authors declare no competing financial interests.

Acknowledgements

This work was partially supported through National Science Foundation grant numbers 1729787 and 1806147. A portion of the STEM experiments was conducted at the Center for Nanophase Materials Sciences at Oak Ridge National Laboratory, which is a Department of Energy (DOE) Office of Science User Facility, through a user project (J.A.H., A.Y.B., J.C.I.). This work used the computational resources of the Extreme Science and Engineering Discovery Environment (XSEDE), which is supported by National Science Foundation grants ACI-1053575 and ACI-1548562. V.R. acknowledges with gratitude the Roma B. and Raymond H. Wittcoff Distinguished University Professorship.

Conflict of Interest

The authors declare no conflict of interest.

Keywords: Bader charge • electrochemistry • oxidative degradation • oxygen reduction reaction • proton exchange membrane fuel cells

- [1] U. S. Drive, Fuel Cell Technical Team Roadmap https://www.energy.gov/sites/prod/files/2017/11/f46/FCTT_Roadmap_Nov_2017_FINAL.pdf (Accessed on 09/06/2018).
- [2] A. Kongkanand, M. F. Mathias, *J. Phys. Chem. Lett.* **2016**, *7*, 1127–1137.
- [3] T. J. Schmidt, H. A. Gasteiger, G. D. Stäb, P. M. Urban, D. M. Kolb, R. J. Behm, *J. Electrochem. Soc.* **1998**, *145*, 2354–2358.
- [4] E. Antolini, E. R. Gonzalez, *Appl. Catal. A* **2009**, *365*, 1–19.
- [5] H. A. Gasteiger, S. S. Kocha, B. Sompalli, F. T. Wagner, *Appl. Catal. B* **2005**, *56*, 9–35.
- [6] A. Kongkanand, M. F. Mathias, *J. Phys. Chem. Lett.* **2016**, *7*, 1127–1137.
- [7] E. Yeager, *J. Mol. Catal.* **1986**, *38*, 5–25.
- [8] R. Jasinski, *Nature* **1964**, *201*, 1212.
- [9] G. Wu, A. Santandreu, W. Kellogg, S. Gupta, O. Ogoke, H. Zhang, H.-L. Wang, L. Dai, *Nano Energy* **2016**, *29*, 83–110.
- [10] M. Chen, J. Liu, W. Zhou, J. Lin, Z. Shen, *Sci. Rep.* **2015**, *5*, 10389.
- [11] D. H. Youn, G. Bae, S. Han, J. Y. Kim, J.-W. Jang, H. Park, S. H. Choi, J. S. Lee, *J. Mater. Chem. A* **2013**, *1*, 8007–8015.
- [12] M. Lefevre, E. Proietti, F. Jaouen, J. P. Dodelet, *Science* **2009**, *324*, 71–74.
- [13] Y. Li, W. Zhou, H. Wang, L. Xie, Y. Liang, F. Wei, J. C. Idrobo, S. J. Pennycook, H. Dai, *Nat. Nanotechnol.* **2012**, *7*, 394–400.
- [14] M. K. Debe, *Nature* **2012**, *486*, 43–51.
- [15] G. Wu, K. L. More, C. M. Johnston, P. Zelenay, *Science* **2011**, *332*, 443–447.
- [16] A. Serov, M. H. Robson, B. Halevi, K. Artyushkova, P. Atanassov, *Electrochim. Commun.* **2012**, *22*, 53–56.
- [17] H. T. Chung, D. A. Cullen, D. Higgins, B. T. Sneed, E. F. Holby, K. L. More, P. Zelenay, *Science* **2017**, *357*, 479–483.
- [18] Y. Zhan, F. Xie, H. Zhang, Z. Lin, J. Huang, W. Zhang, X. Sun, Y. Zhang, J. Chen, H. Meng, *J. Electrochem. Soc.* **2018**, *165*, J3008–J3015.
- [19] K. Singh, F. Razmjoei, J.-S. Yu, *J. Mater. Chem. A* **2017**, *5*, 20095–20119.
- [20] X. Xie, C. He, B. Li, Y. He, D. A. Cullen, E. C. Wegener, A. J. Kropf, U. Martinez, Y. Cheng, M. H. Engelhard, M. E. Bowden, M. Song, T. Lemmon, X. S. Li, Z. Nie, J. Liu, D. J. Myers, P. Zelenay, G. Wang, G. Wu, V. Ramani, Y. Shao, *Nat. Catal.* **2020**, *3*, 1044–1054.
- [21] X. X. Wang, D. A. Cullen, Y.-T. Pan, S. Hwang, M. Wang, Z. Feng, J. Wang, M. H. Engelhard, H. Zhang, Y. He, Y. Shao, D. Su, K. L. More, J. S. Spendelow, G. Wu, *Adv. Mater.* **2018**, *30*, 1706758.
- [22] L. Yang, D. Cheng, H. Xu, X. Zeng, X. Wan, J. Shui, Z. Xiang, D. Cao, *Proc. Natl. Acad. Sci. USA* **2018**, *115*, 6626–6631.
- [23] O. Gröger, H. A. Gasteiger, J.-P. Suchsland, *J. Electrochem. Soc.* **2015**, *162*, A2605-A2622.
- [24] C. Takei, K. Kakinuma, K. Kawashima, K. Tashiro, M. Watanabe, M. Uchida, *J. Power Sources* **2016**, *324*, 729–737.
- [25] A. Serov, M. J. Workman, K. Artyushkova, P. Atanassov, G. McCool, S. McKinney, H. Romero, B. Halevi, T. Stephenson, *J. Power Sources* **2016**, *327*, 557–564.
- [26] C. H. Choi, C. Baldizzone, J.-P. Grote, A. K. Schuppert, F. Jaouen, K. J. J. Mayrhofer, *Angew. Chem. Int. Ed.* **2015**, *54*, 12753–12757; *Angew. Chem.* **2015**, *127*, 12944–12948.
- [27] L. Castanheira, W. O. Silva, F. H. B. Lima, A. Crisci, L. Dubau, F. Maillard, *ACS Catal.* **2015**, *5*, 2184–2194.
- [28] P. T. Yu, W. Gu, R. Makharla, F. T. Wagner, H. A. Gasteiger, *ECS Trans.* **2006**, *3*, 797–809.
- [29] M. P. Karthikayini, T. Thirupathi, G. Wang, V. K. Ramani, R. K. Raman, *J. Electrochem. Soc.* **2016**, *163*, F539-F547.
- [30] J. Parrondo, T. Han, E. Niangar, C. Wang, N. Dale, K. Adjeman, V. Ramani, *Proc. Natl. Acad. Sci. USA* **2014**, *111*, 45–50.
- [31] C.-P. Lo, G. Wang, A. Kumar, V. Ramani, *Appl. Catal. B* **2013**, *140*–141, 133–140.
- [32] A. Kumar, V. Ramani, *ACS Catal.* **2014**, *4*, 1516–1525.
- [33] V. T. Thanh Ho, K. C. Pillai, H.-L. Chou, C.-J. Pan, J. Rick, W.-N. Su, B.-J. Hwang, J.-F. Lee, H.-S. Sheu, W.-T. Chuang, *Energy Environ. Sci.* **2011**, *4*, 4194.
- [34] C. He, S. Sankarasubramanian, I. Matanovic, P. Atanassov, V. Ramani, *ChemSusChem* **2019**, *12*, 3468–3480.
- [35] C. He, X. Wang, S. Sankarasubramanian, A. Yadav, K. Bhattacharyya, X. Liang, V. Ramani, *ACS Appl. Mater. Interfaces* **2020**, *3*, 5774–5783.
- [36] C. He, S. Sankarasubramanian, A. Ellis, J. Parrondo, C. Gumeci, M. Kodali, I. Matanovic, A. K. Yadav, K. Bhattacharyya, N. Dale, P. Atanassov, V. K. Ramani, *ACS Catal.* **2021**, *11*, 7006–7017.
- [37] E. F. Holby, P. Zelenay, *Nano Energy* **2016**, *29*, 54–64.
- [38] S. Kattel, P. Atanassov, B. Kiefer, *Phys. Chem. Chem. Phys.* **2014**, *16*, 13800–13806.
- [39] Y. Zhong, X. Xia, F. Shi, J. Zhan, J. Tu, H. J. Fan, *Adv. Sci.* **2016**, *3*, 1500286.
- [40] J. Li, S. Ghoshal, W. Liang, M.-T. Sougrati, F. Jaouen, B. Halevi, S. McKinney, G. McCool, C. Ma, X. Yuan, Z.-F. Ma, S. Mukerjee, Q. Jia, *Energy Environ. Sci.* **2016**, *9*, 2418–2432.
- [41] A. Serov, K. Artyushkova, P. Atanassov, *Adv. Energy Mater.* **2014**, *4*, 1301735.
- [42] K. Strickland, E. Miner, Q. Jia, U. Tylus, N. Ramaswamy, W. Liang, M.-T. Sougrati, F. Jaouen, S. Mukerjee, *Nat. Commun.* **2015**, *6*, 7343.
- [43] DOE U.S. DRIVE Fuel Cell Tech Team, Cell component accelerated stress test and polarization curve protocols for PEM fuel cells, **2013**.
- [44] Y. C. Kimmel, X. Xu, W. Yu, X. Yang, J. G. Chen, *ACS Catal.* **2014**, *4*, 1558–1562.
- [45] S. M. Song, J. K. Park, O. J. Sul, B. J. Cho, *Nano Lett.* **2012**, *12*, 3887–3892.
- [46] J. F. Shackelford, Y.-H. Han, S. Kim, S.-H. Kwon, *Materials Science and Engineering Handbook*, CRC Press, **2015**.
- [47] J. A. Rodriguez, P. Liu, Y. Takahashi, F. Viñes, L. Feria, E. Florez, K. Nakamura, F. Illas, *Catal. Today* **2011**, *166*, 2–9.
- [48] J. A. Rodriguez, J. Evans, L. Feria, A. B. Vidal, P. Liu, K. Nakamura, F. Illas, *J. Catal.* **2013**, *307*, 162–169.
- [49] S. Kattel, G. Wang, *J. Mater. Chem. A* **2013**, *1*, 10790–10797.
- [50] P. Sabatier, *Ber. Dtsch. Chem. Ges.* **1911**, *44*, 1984–2001.
- [51] J. K. Nørskov, J. Rossmeisl, A. Logadottir, L. Lindqvist, J. R. Kitchin, T. Bligaard, H. Jónsson, *J. Phys. Chem. B* **2004**, *108*, 17886–17892.
- [52] C. G. Vayenas, S. Bebelis, S. Ladas, *Nature* **1990**, *343*, 625–627.
- [53] M. Asadi, K. Kim, C. Liu, A. V. Addepalli, P. Abbas, P. Yasaei, P. Phillips, A. Behrangiinia, J. M. Cerrato, R. Haasch, P. Zapol, B. Kumar, R. F. Klie, J. Abiade, L. A. Curtiss, A. Salehi-Khojin, *Science* **2016**, *353*, 467–470.
- [54] J. K. Nørskov, T. Bligaard, J. Rossmeisl, C. H. Christensen, *Nat. Chem.* **2009**, *1*, 37–46.
- [55] W. Tang, E. Sanville, G. Henkelman, *J. Phys. Condens. Matter* **2009**, *21*, 084204.
- [56] A. Serov, M. H. Robson, M. Smolnik, P. Atanassov, *Electrochim. Acta* **2013**, *109*, 433–439.
- [57] W. Ju, A. Bagger, G.-P. Hao, A. S. Varela, I. Sinev, V. Bon, B. Roldan Cuena, S. Kaskel, J. Rossmeisl, P. Strasser, *Nat. Commun.* **2017**, *8*, 944.
- [58] T. Muneshwar, K. Cadien, *Appl. Surf. Sci.* **2018**, *435*, 367–376.

- [59] D. Jaeger, J. Patscheider, *J. Electron Spectrosc. Relat. Phenom.* **2012**, *185*, 523–534.
- [60] S. J. Pennycook, D. E. Jesson, *Ultramicroscopy* **1991**, *37*, 14–38.
- [61] A. Holewinski, J. C. Idrobo, S. Linic, *Nat. Chem.* **2014**, *6*, 828–834.
- [62] C. A. Reiser, L. Bregoli, T. W. Patterson, J. S. Yi, J. D. Yang, M. L. Perry, T. D. Jarvi, *Electrochem. Solid-State Lett.* **2005**, *8*, A273–A276.
- [63] A. J. Bard, L. R. Faulkner, *Electrochemical Methods: Fundamentals and Applications*, 2nd ed., Wiley, 2001.
- [64] D. E. Beltrán, S. Litster, *ACS Energy Lett.* **2019**, *4*, 1158–1161.
- [65] G. Kresse, J. Furthmüller, *Phys. Rev. B* **1996**, *54*, 11169.
- [66] P. E. Blöchl, *Phys. Rev. B* **1994**, *50*, 17953.
- [67] J. P. Perdew, K. Burke, M. Ernzerhof, *Phys. Rev. Lett.* **1996**, *77*, 3865–3868.
- [68] H. J. Monkhorst, J. D. Pack, *Phys. Rev. B* **1976**, *13*, 5188.
- [69] K. Reuter, M. Scheffler, *Phys. Rev. B* **2001**, *65*, 035406.
- [70] M. Bosman, M. Watanabe, D. Alexander, V. Keast, *Ultramicroscopy* **2006**, *106*, 1024–1032.

Manuscript received: June 28, 2021
Revised manuscript received: August 10, 2021
Accepted manuscript online: August 12, 2021
Version of record online: September 22, 2021